Check for updates

Multispectral graphene-based electro-optical surfaces with reversible tunability from visible to microwave wavelengths

M. Said Ergoktas [1,2], Gokhan Bakan[1,2], Evgeniya Kovalska[3], Lewis W. Le Fevre[2,4,5], Richard P. Fields[2], Pietro Steiner [1,2], Xiaoxiao Yu [1,2], Omer Salihoglu[3], Sinan Balci [6], Vladimir I. Fal'ko [2,7,8], Kostya S. Novoselov [2,7], Robert A. W. Dryfe [2,4,8] and Coskun Kocabas [1,2,8] ✉

Optical materials with colour changing abilities have been explored for use in display devices[1], smart windows[2,3] or in the modulation of visual appearance[4-6]. The efficiency of these materials, however, has strong wavelength dependence, which limits their functionality to a specific spectral range. Here, we report graphene-based electro-optical devices with unprecedented optical tunability covering the entire electromagnetic spectrum from the visible to microwave. We achieve this non-volatile and reversible tunability by electro-intercalation of lithium into graphene layers in an optically accessible device structure. The unique colour changing capability, together with area-selective intercalation, inspires the fabrication of new multispectral devices, including display devices and electro-optical camouflage coating. We anticipate that these results provide realistic approaches for programmable smart optical surfaces with a potential utility in many scientific and engineering fields such as active plasmonics and adaptive thermal management.

Conventional optoelectronic devices, such as light sources and detectors, are intentionally designed to operate in a certain wavelength range to achieve the highest efficiency. There might be new opportunities for optoelectronic devices that can operate over seemingly unrelated wavelengths such as the visible and terahertz, whose energies differ by three orders of magnitude. Applications that could exploit these multispectral operations include adaptive camouflage coatings that can perform concealment both in the visible and infrared wavelengths, a display device that can encode information in different wavelengths or a dynamic thermal blanket that can selectively reflect visible or infrared light. Such multispectral devices may be possible if they can overcome the existing challenges of requiring (1) broadband electro-optical tunability, (2) a multispectral device structure and (3) non-volatile switching. Research on tunable optical materials has primarily focused on controlling the state of materials to alter the optical response. Phase-change[7–9] and electrochromic[10,11] materials are two examples capable of a colour change triggered by a change in temperature or an electric field. However, existing device structures that require a conductive top electrode, for example, are limited in their spectral operation range and utility for multispectral applications[12,13].

Electro-intercalation of atomic or molecular ions into layered materials, such as graphite intercalation compounds (GICs), can rise to the challenge by providing the host material with a new means of controlling its electrical, optical, thermal and magnetic properties[14–17]. However, tuning the optical properties of the host material via intercalation has been overlooked, mainly because of the difficulties of integrating optical devices with electrochemical cells[17,18]. In this Letter, we report an electrochemical optical platform with non-volatile and reversible reflectivity modulation covering the entire electromagnetic spectrum from the visible to microwave regime. This platform differs from previously reported graphene devices, which are designed primarily for specific wavelength ranges (microwave[19], terahertz[20], infrared[5,6] and visible[21]) using single and multilayer graphene. Overcoming the challenge of extending the coverage to the visible while keeping the optical activity at longer wavelengths has led to the innovative device structure reported here, reaching the ultimate multispectral operation.

Figure 1a illustrates the structure of the device and its operation principle. The device takes advantage of multilayer graphene (MLG, ~150 layers) as the anode as well as the optically active material. The number of graphene layers is estimated using visible–near-infrared (NIR) transmission measurements and optical modelling (Supplementary Note 1 and Supplementary Fig. 1). The high electrical conductivity of MLG ($<50\,\Omega\,sq^{-1}$) eliminates the requirement for an additional top electrode layer. The key feature of the device is that the MLG is optically accessible under a transparent protection layer. This is achieved by laminating MLG and vacuum sealing the device in a low-density polyethylene pouch (LDPE, with a density of 0.91–$0.94\,g\,cm^{-3}$ and crystallinity of 42–62%) that has over 90% optical transparency from the visible to microwave wavelengths, except for the infrared absorptions in the fingerprint region (Supplementary Fig. 2). The airtight packaging is crucial for stable non-volatile operation. Aluminium foil, coated with lithium-doped nickel manganese cobalt oxide (NMC), is used as the cathode and the source of Li+ ions. Electro-intercalation of Li+ ions into the MLG (charging the device) is achieved by applying a constant electric current ($~1\,mA\,cm^{-2}$) towards the cathode (Fig. 1b). The device voltage was monitored to track the state of charge (SoC). Reversing the current direction, or simply shorting through an electrical load
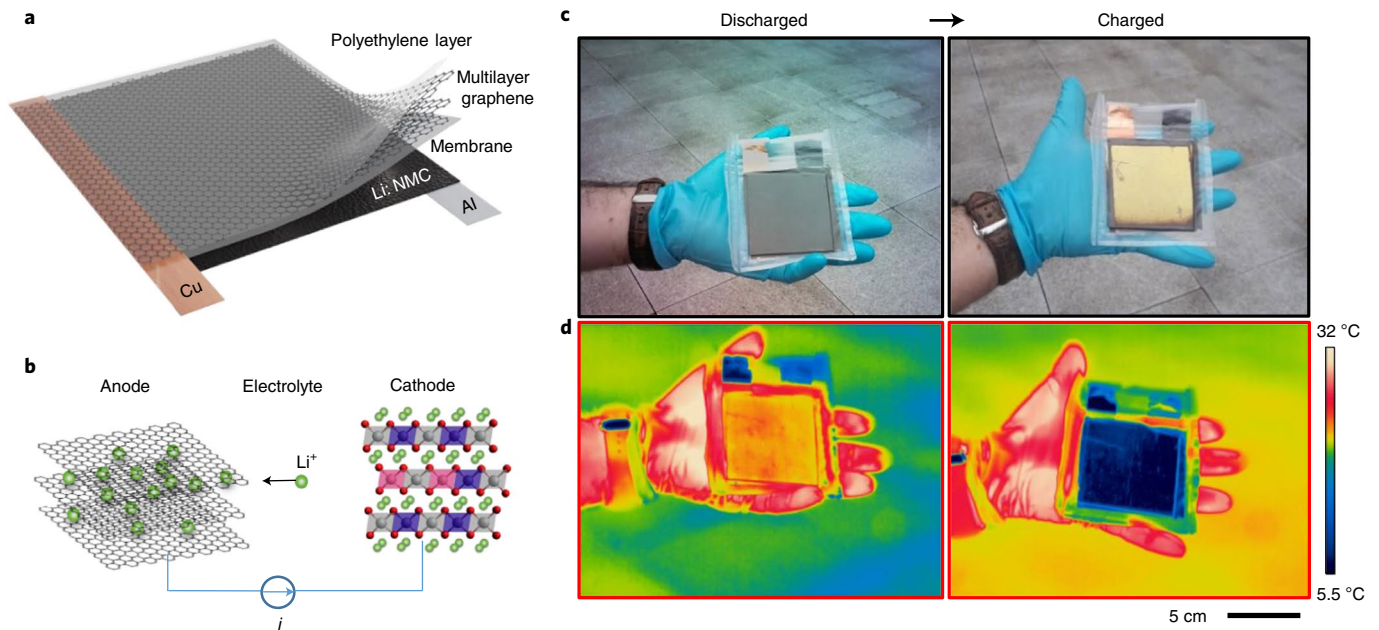
Fig. 1 | Device structure and operation principle. a, Schematic of the device, which consists of the PE protection layer, MLG (anode), an electrolyte-containing membrane and aluminium foil coated with lithium-doped NMC (cathode). **b**, Illustration of Li⁺ ion intercalation into the graphene layers. **c,d**, Visible (**c**) and infrared (**d**) images of the device in fully discharged and charged states, showing non-volatile multispectral tunability.

(Supplementary Fig. 3 and Supplementary Video 1), de-intercalates the ions from the MLG, making the operation reversible and repeatable[22]. During intercalation (or de-intercalation), the optical properties of MLG change drastically. The discharged device appears dark grey due to the high absorptivity (>80%) of the top graphene layer in the visible regime. When the device is fully charged (at ~3.8 V), the graphene layer appears gold in colour (Fig. 1c), similar to a stage-1 GIC[16,23]. The achievable colour space can be enriched to include a range from red to blue using optical effects such as thin-film interference (Supplementary Note 2 and Supplementary Figs. 4 and 5). This can lead to the generation of arbitrary colours using subpixels and varying the optical reflectivity with SoC in a similar way as is employed by display devices. Besides the visible colour change, the infrared properties follow a similar trend and exhibit low reflectivity ($R \approx 30\%$), and hence high emissivity ($\varepsilon \approx 0.7$), when discharged, and high reflectivity ($R \approx 75\%$), and hence low emissivity ($\varepsilon \approx 0.25$), when charged (Fig. 1d). Thermal imaging of the device was performed outdoors to minimize the ambient thermal emission reflected from the device. The charged device appears colder (<5 °C) to the thermal camera compared to its actual temperature because of its low infrared emissivity. The device operation resembles that of Li-ion batteries with a coulombic efficiency of over 85% for more than 2,200 charge/discharge cycles (Supplementary Fig. 6).

To examine the multispectral response, we measured the reflection spectra of the devices at different doping levels. By combining the reflection measurements from three different spectrometers (ultraviolet (UV)/visible/NIR, Fourier-transform infrared (FTIR) and time-domain terahertz spectrometers), we obtained a reflectivity change from the UV ($\lambda = 300$ nm) to microwave ($\lambda = 3$ mm) as shown in Fig. 2a. The reflectivity can be modulated in the entire range of the non-ionizing part of the electromagnetic spectrum. Figure 2b compares the reflectivity modulation for three sample wavelengths from the visible ($\lambda = 500$ nm), infrared ($\lambda = 10$ μm) and terahertz ($\lambda = 1$ mm) regimes. The modulation onset varies with the wavelength of the light. The terahertz reflectivity increases at a SoC of ~0.05, whereas the modulation in the infrared and visible regime starts appearing at ~0.2 and ~0.4 SoC, respectively. The sharp drop

in the reflectance is an indicator of the free-carrier plasma resonance, ω_p. This reflection minimum shifts from the far-infrared to the UV with increasing doping. The experimental spectra can be modelled using intraband (Drude) and interband optical conductivity, $\varepsilon = \varepsilon_\infty + \varepsilon_{int} + i\frac{\omega_p^2 \tau}{\omega(1 - i\omega\tau)}$, where ε_∞ is the background dielectric constant, ε_{int} accounts for the contribution of interband transitions, τ is the scattering time of the carriers and ω is the angular frequency of light (Supplementary Note 3 and Supplementary Fig. 7). Fitting the model to the reflectivity measurements shows that the plasma frequency varies from 0.1 to 9 eV (Fig. 2c) and the scattering time from 30 to 1 fs with charging (Supplementary Fig. 8). At higher doping levels, stage-1 and stage-2 intercalated graphitic compounds have a smaller scattering time (10–20 fs) due to additional scattering from intercalated ions and electron–electron scattering[24]. For the same device structure, Fig. 2d shows the variation in the sheet resistance of the MLG and the device voltage during a charging cycle. Clear steps are observed in these measurements, indicating the distinct intercalation stages.

For more insights into the intercalation process, we performed in situ Raman and photoluminescence measurements (excitations of 633 nm and 457 nm) during the charging and discharging cycles (Supplementary Note 4 provides the complete Raman analysis). Figure 3a–c shows the doping-induced changes in the possible Raman pathways for the G and 2D bands. As we charge the device, the Raman G band at 1,581 cm⁻¹ first shifts to 1,590 cm⁻¹ due to the Kohn anomaly[25–27] and splits into two peaks[28], then disappears due to Pauli blocking[29] of the Raman pathways. Similarly, the intensity of the 2D band decreases gradually and disappears at relatively lower voltages (~3.48 V; Fig. 3d). We also observed hot luminescence from heavily doped MLG at energies <$2E_F$, where excited-state relaxation pathways become available. The hot luminescence also disappears due to the Pauli blocking of the laser excitation (Fig. 3e). We extract the Fermi energy, E_F (Fig. 3f), using the onset and cutoff of the hot luminescence, the Pauli blocking condition for the G band ($2E_F = E_{ex}$) and for the 2D band ($2E_F = E_{ex} - 2\hbar\Omega_D$), where E_{ex} is the excitation energy and Ω_D the energy of the D-band phonons. These results are in good agreement with the Fermi energy extracted from
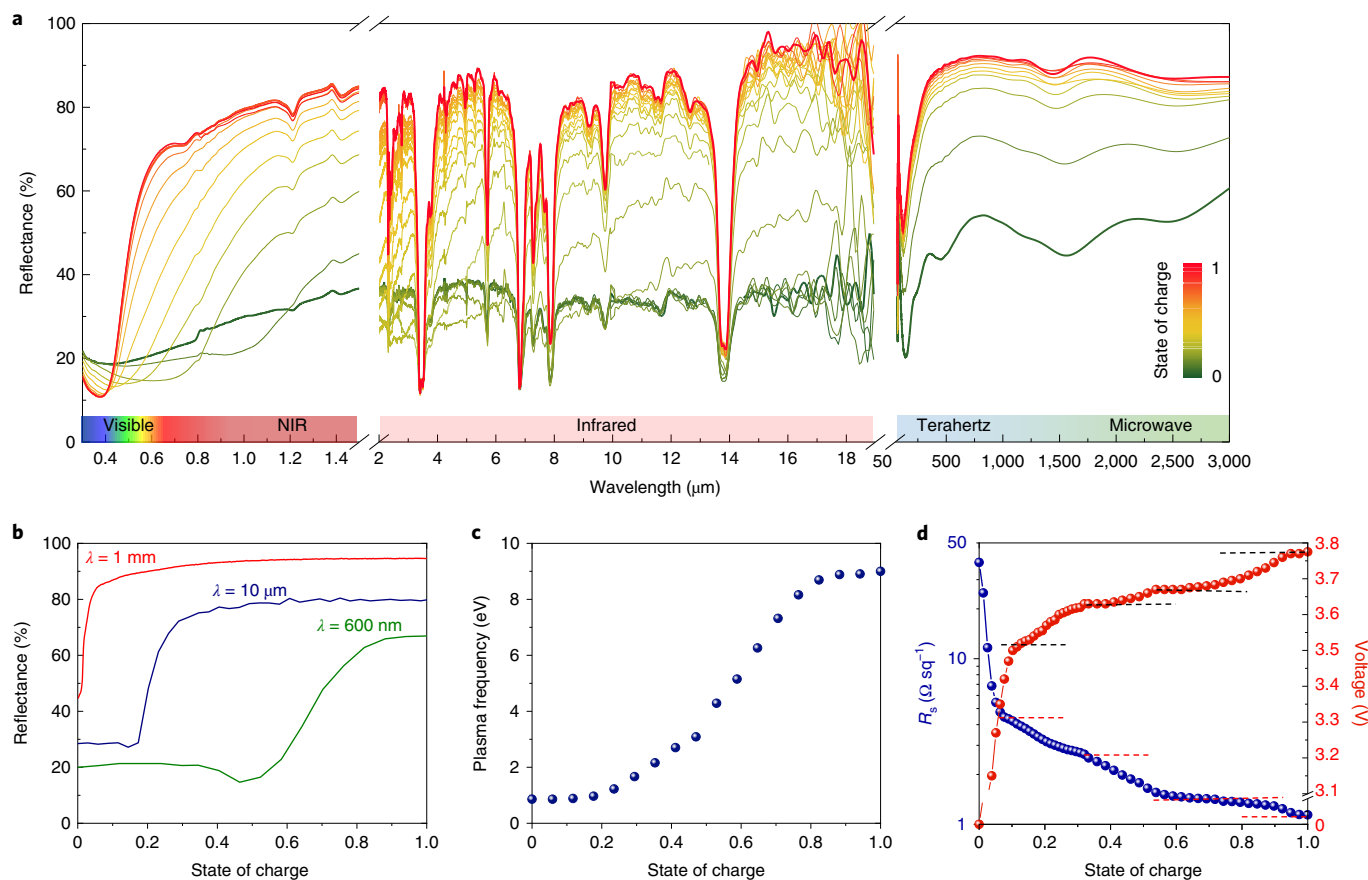
Fig. 2 | Multispectral tunability from the visible to microwave. a, Measured reflection spectra covering the visible, infrared, terahertz and microwave regimes for different doping levels (state of charge). The general trend is increasing reflectance with increasing SoC. The sharp reflection dips in the infrared spectrum are due to absorption by the top PE protection layer. **b**, Variation in the reflectivity of the device at the selected wavelengths of 600 nm, 10 μm and 1 mm. **c**, Change in the plasma frequency as a function of the SoC. **d**, Device voltage and sheet resistance of the MLG during charging. Dashed lines mark the different stages of the lithiation of the graphene.

optical transmission measurements (Fig. 3f). Our results show that the Fermi energy of the MLG can be reversibly increased up to 1.5 eV, which is consistent with band-structure calculations for LiC$_6$ (ref. [30]). Raman analysis also shows that the graphene layer stays intact even after 20,000 intercalation/de-intercalation cycles, suggesting that the degradation of the devices is not due to structural damage to the graphene layer, but is instead due to the loss of Li ions on the cathode electrode (Supplementary Fig. 19).

To show the promise of the tunable multispectral optical surfaces, we demonstrate two proof-of-concept (PoC) devices. The first is a display capable of showing images in the visible, infrared and terahertz wavelengths, simultaneously. Figure 4a presents a cross-sectional illustration of the device, which includes a continuous graphene layer and area-selective intercalation of Li$^+$ ions enabled by patterning the cathode. Controlling the voltage applied to an individual electrode enables variation of the pixel's spectral response. Figure 4b showcases the display device, with its back electrode patterned into the letters 'N', 'G' and 'I' (the initials of the National Graphene Institute). Multispectral imaging of the device was performed by a complementary metal–oxide–semiconductor camera operating in the visible regime (400–700 nm), a long-wave infrared camera (8–13 μm) and a terahertz raster-scan imaging system (0.5–2 THz). Applying 3.8, 3.5 and 3.3 V to the 'N', 'G' and 'I' pixels, respectively, revealed 'N' at all wavelengths, 'G' in the infrared and terahertz and 'I' only in the terahertz. Beyond the demonstrated function as a multispectral display, it has the potential to be

used for optical security applications in which an encoded message can only be revealed with the correct key that corresponds to applying a specific voltage to the device and imaging in a specific range of wavelengths for our technology. The demonstrated concept relies on non-overlapping voltage ranges for different spectral regimes—for example, being able to change the infrared emission while maintaining the visible response. This feature is visualized on a device by (1) changing both the visible and infrared response, (2) changing only the infrared response while the visible reflection is always low and (3) changing only the visible response while the infrared emission is always low (Supplementary Video 2). The devices leverage flexible printed circuit board technology to build flexible, multipixel and multispectral displays (Supplementary Fig. 22).

The second PoC device is a multispectral adaptive camouflage system that has a unique capability of dynamically modifying its visible and infrared appearance. The adaptive visibility was achieved by patterning the back electrode into a camouflage pattern. Then, specific parts of the device were activated to match the appearance to that of a spatially varying background (Fig. 4c). The graph in Fig. 4c shows a time trace of the red, green and blue (RGB) colour indices during adaptation. The adaptation capabilities of these optical surfaces can be improved by integrating pixelated devices with visual feedback. Similarly, the device can adapt its thermal appearance. Figure 4d,e shows thermal images of a device as it adapts its infrared emission to cold and hot backgrounds (Supplementary Video 3). These demonstrations highlight a comprehensive case of thermal
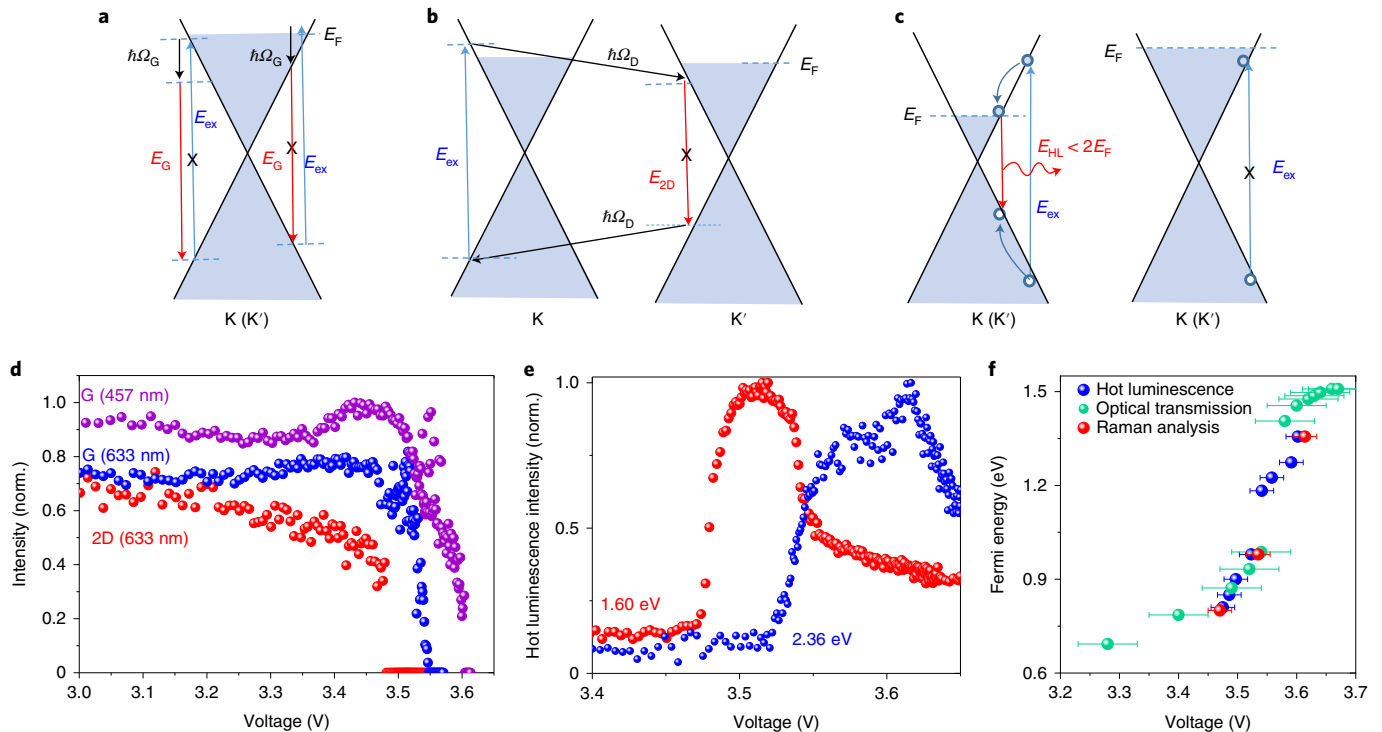
Fig. 3 | In situ Raman characterization of the intercalation process. a,b, Illustration of the gate-induced change in possible Raman pathways for the G (**a**) and 2D (**b**) bands. **c**, Illustration of hot electron photoluminescence pathways in doped MLG and its Pauli blocking condition. **d**, Variation of the Raman intensity of the G and 2D peaks as a function of voltage. **e**, Voltage dependence of hot luminescence from MLG at energies of 1.60 and 2.36 eV. **f**, Voltage dependence of the Fermi energy of MLG extracted from the Pauli blocking conditions of the Raman peaks, hot luminescence and optical transmission. The error bars indicate the uncertainty in obtaining the voltage values for the Pauli blocking condition.

camouflage where the background infrared emission changes dynamically, taking into account moving targets and changing environmental factors, such as ambient temperature and clouds (Supplementary Note 5 provides further discussions). Although the background in these examples was kept spatially uniform, we have demonstrated that the approach used for visible camouflage can be adapted to a spatially varying thermal background (Supplementary Fig. 23). A time trace of the infrared camouflage process reveals the high transition speed (~1 s) and quantifies how well the infrared emission from the device (rendered as the apparent temperature by the camera) adapts to the background (shaded areas, Fig. 4d,e). The camouflage operation can be extended easily into the mid-wave (3–5 μm) and short-wave (1.4–3 μm) infrared regimes, as the emissivity modulation covers the entire infrared spectrum (Supplementary Fig. 24). We also performed benchmarking studies of our devices against existing thermal metamaterials and other variable-emissivity technologies. The key device metrics for cloaking applications are tuning mechanism, response time and power consumption (Supplementary Note 6 and Supplementary Table 2).

We next discuss how the multispectral tunability can improve adaptive thermal management of satellites in outer space by balancing the absorbed solar radiation (wavelength range of 0.3–2.5 μm) and the internal heat generated by satellite electronics with the emitted infrared radiation (peaks of ~10 μm) (Fig. 5a–c). Maintaining this balance with passive optical components while a satellite orbits the Earth is a major design challenge, especially for small satellites[31]. The multispectral electro-optical tunability in the visible and infrared regimes demonstrated here can address this need by varying the visible absorptivity and infrared emissivity with the SoC (Fig. 5d). For the calculations, we used a low-orbit (altitude of 600 km) CubeSat as a model system for two extreme cases: the satellite exposed to direct sunlight (Fig. 5a(i)) and the satellite in Earth's

shadow (Fig. 5a(ii)). In the first case, rejecting the incident solar irradiance is the priority, as the solar irradiance in the satellite's orbit (~1,347 W m⁻²) is much larger than a blackbody at 30 °C can emit to deep space (~479 W m⁻²). Varying the SoC on the surfaces that are not exposed to sunlight provides a dynamic net cooling rate as large as 141 W m⁻². In the second case, all sides but the Earth-facing one are exposed to deep space, and the satellite receives no direct or indirect solar radiation. The net cooling rate in this case is evaluated to be between 95 and 282 W m⁻² with varying SoC (Fig. 5e). By contrast, a thermal coating with static optical properties can only provide a static cooling rate, making the satellite prone to larger temperature fluctuations as the satellite position and activity vary ($\Delta T \approx 6\,°C$ for static versus 0 °C for our coating; for a detailed analysis see Supplementary Note 7).

The temporal response of the device is of critical importance for these applications. The switching speed is limited by the intercalation process, quantified as the SoC in this work, which has a linear dependence on the device current. For a moderate current density of ~1 mA cm⁻², full charging and the accompanying optical changes take place in ~40 s, which is superior to the electrochromic alternatives operating in the visible regime with switching durations ranging from tens of seconds to minutes[10]. Switching the terahertz and infrared response is faster in comparison, with a response time on the order of 1 s and a few seconds, respectively (Supplementary Note 8 and Supplementary Fig. 26).

The long-term steady operation of the devices requires maintaining the initial purity of the electrolytes, specifically the low moisture (<15 ppm) and hydrogen fluoride (HF) (<50 ppm) contents. The same problem for Li-ion batteries is solved by airtight packing and a solid-electrolyte interface[32]. Following this example, our devices were vacuum-sealed in PE pouches to press all layers against each other while keeping the graphene layers optically accessible.
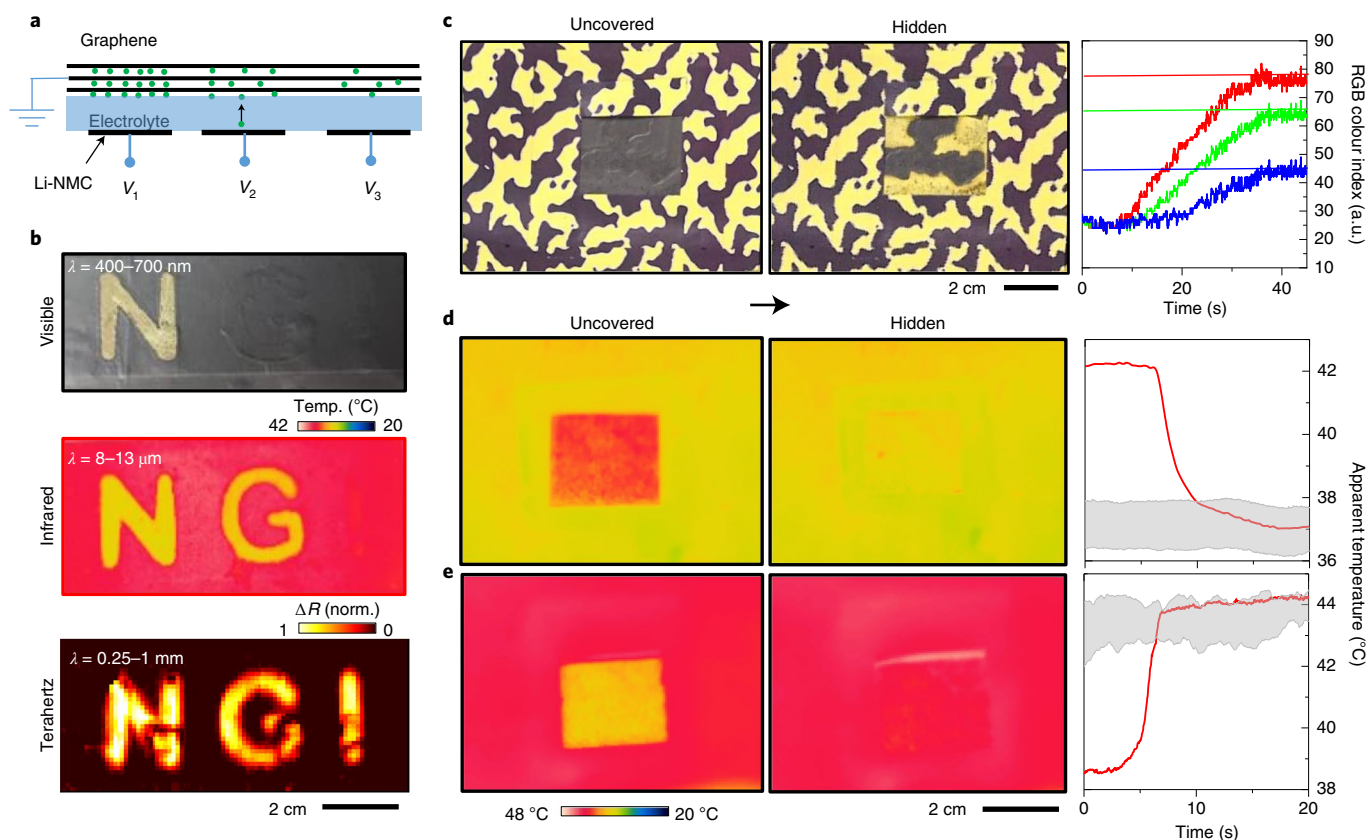
Fig. 4 | Multispectral display and adaptive camouflage. a, Cross-sectional illustration of a PoC multispectral display based on area-selective lithiation. Patterned cathodes define individually addressable pixels. The state of charge determines the operation wavelength. **b**, Images of a display device rendered in the visible, infrared and terahertz regimes. **c**, Demonstration of adaptive visible camouflage. The device blends into a spatially varying background by matching its visible appearance. The graph shows the change in RGB colour indices from the active region of the device as it blends in. Horizontal lines mark the background RGB indices. **d,e**, Demonstration of adaptive infrared camouflage. The device can adapt its infrared emission to blend into cold (**d**) and hot (**e**) backgrounds. The graphs show the time traces of the apparent device temperature during adaptation. The shaded areas show the background temperature range.

The endurance of the devices was tested in the terahertz, infrared and visible regimes. The results show that the devices can operate for more than 11,000, 2,200 and 580 on/off cycles in these regimes, respectively (Supplementary Figs. 27–29 and Supplementary Note 9). Thanks to the recent advances in graphene growth, we anticipate that these devices are compatible with large-scale production (Supplementary Fig. 30). Beyond the PoC demonstrations included here, the developed technology will inspire new applications, for example as a battery level indicator for Li-ion batteries (Supplementary Fig. 31).

In conclusion, we have demonstrated multispectral electro-optical devices operating over the entire electromagnetic spectrum from the visible to microwave. This unprecedented capability will inspire new technologies with very high potential to reshape tunable optics either as a standalone unit or by incorporation with established light-manipulation approaches. Furthermore, the demonstrated broad electro-optical tunability of the plasma frequency yields an electrically tunable plasmonic system that will enable multispectral active plasmonics.

Online content

Any methods, additional references, Nature Research reporting summaries, source data, extended data, supplementary information, acknowledgements, peer review information; details of author contributions and competing interests; and statements of data and code availability are available at https://doi.org/10.1038/s41566-021-00791-1.

References
1. Hosseini, P., Wright, C. D. & Bhaskaran, H. An optoelectronic framework enabled by low-dimensional phase-change films. *Nature* **511**, 206–211 (2014).
2. Lin, J. et al. Thermochromic halide perovskite solar cells. *Nat. Mater.* **17**, 261–267 (2018).
3. Montelongo, Y. et al. Electrotunable nanoplasmonic liquid mirror. *Nat. Mater.* **16**, 1127–1135 (2017).
4. Yu, C. et al. Adaptive optoelectronic camouflage systems with designs inspired by cephalopod skins. *Proc. Natl Acad. Sci. USA* **111**, 12998–13003 (2014).
5. Salihoglu, O. et al. Graphene-based adaptive thermal camouflage. *Nano Lett.* **18**, 4541–4548 (2018).
6. Ergoktas, M. S. et al. Graphene-enabled adaptive infrared textiles. *Nano Lett.* **20**, 5346–5352 (2020).
7. Wuttig, M., Bhaskaran, H. & Taubner, T. Phase-change materials for non-volatile photonic applications. *Nat. Photon* **11**, 465–476 (2017).
8. Zhang, Y. et al. Broadband transparent optical phase change materials for high-performance nonvolatile photonics. *Nat. Commun.* **10**, 4279 (2019).
9. Bakan, G., Ayas, S., Saidzoda, T., Celebi, K. & Dana, A. Ultrathin phase-change coatings on metals for electrothermally tunable colors. *Appl. Phys. Lett.* **109**, 071109 (2016).
10. Granqvist, C. G. et al. Electrochromic materials and devices for energy efficiency and human comfort in buildings: a critical review. *Electrochim. Acta* **259**, 1170–1182 (2018).
11. Lu, N. et al. Electric-field control of tri-state phase transformation with a selective dual-ion switch. *Nature* **546**, 124–128 (2017).

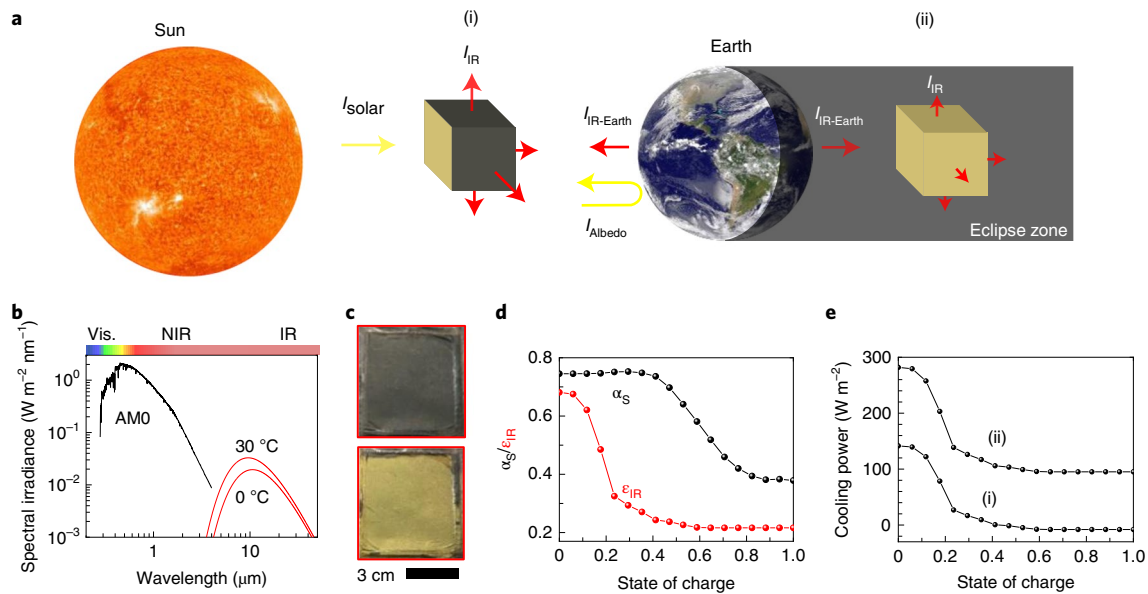**Fig. 5 | Adaptive thermal management for satellites. a**, Schematic of a CubeSat orbiting the Earth, illustrating the solar and infrared irradiance on it. Sun and Earth images by NASA are licensed under CC BY 2.0 (http://creativecommons.org/licenses/by/2.0/). **b**, Spectral solar irradiance (black line) on a low-Earth-orbiting satellite and blackbody radiation at 0 and 30 °C (red lines). **c**, Photographs of a large-area device at zero and full state of charge. This device can fully cover a single side of a CubeSat. **d**, Weighted solar absorptivity α_S (black line) and infrared emissivity ε_{IR} (red line) of the developed multispectral surfaces as a function of SoC. **e**, Calculated cooling power of the satellite under direct sunlight (**a**(i)) and in Earth's shadow (**a**(ii)).

12. Llordés, A., Garcia, G., Gazquez, J. & Milliron, D. J. Tunable near-infrared and visible-light transmittance in nanocrystal-in-glass composites. *Nature* **500**, 323–326 (2013).

13. Runnerstrom, E. L., Llordés, A., Lounis, S. D. & Milliron, D. J. Nanostructured electrochromic smart windows: traditional materials and NIR-selective plasmonic nanocrystals. *Chem. Commun.* **50**, 10555–10572 (2014).

14. Daukiya, L. et al. Functionalization of 2D materials by intercalation. *Prog. Surf. Sci.* **94**, 1–20 (2019).

15. Wan, J. et al. Tuning two-dimensional nanomaterials by intercalation: materials, properties and applications. *Chem. Soc. Rev.* **45**, 6742–6765 (2016).

16. Dresselhaus, M. S. & Dresselhaus, G. Intercalation compounds of graphite. *Adv. Phys.* **30**, 139–326 (1981).

17. Bao, W. et al. Approaching the limits of transparency and conductivity in graphitic materials through lithium intercalation. *Nat. Commun.* **5**, 4224 (2014).

18. Pfluger, P., Künzi, H. U. & Güntherodt, H. Discovery of a new reversible electrochromic effect. *Appl. Phys. Lett.* **35**, 771–772 (1979).

19. Balci, O., Polat, E. O., Kakenov, N. & Kocabas, C. Graphene-enabled electrically switchable radar-absorbing surfaces. *Nat. Commun.* **6**, 6628 (2015).

20. Kakenov, N. et al. Observation of gate-tunable coherent perfect absorption of terahertz radiation in graphene. *ACS Photonics* **3**, 1531–1535 (2016).

21. Polat, E. O. et al. Graphene-enabled optoelectronics on paper. *ACS Photonics* **3**, 964–971 (2016).

22. Xiao, J. et al. Understanding and applying coulombic efficiency in lithium metal batteries. *Nat. Energy* **5**, 561–568 (2020).

23. Lodico, J. J. et al. Irreversibility at macromolecular scales in the flake graphite of the lithium-ion battery anode. *J. Power Sources* **436**, 226841 (2019).

24. Brida, D. et al. Ultrafast collinear scattering and carrier multiplication in graphene. *Nat. Commun.* **4**, 1987 (2013).

25. Piscanec, S., Lazzeri, M., Mauri, F., Ferrari, A. C. & Robertson, J. Kohn anomalies and electron–phonon interactions in graphite. *Phys. Rev. Lett.* **93**, 185503 (2004).

26. Pisana, S. et al. Breakdown of the adiabatic Born–Oppenheimer approximation in graphene. *Nat. Mater.* **6**, 198–201 (2007).

27. Das, A. et al. Monitoring dopants by Raman scattering in an electrochemically top-gated graphene transistor. *Nat. Nanotechnol.* **3**, 210–215 (2008).

28. Sole, C., Drewett, N. E. & Hardwick, L. J. Insitu Raman study of lithium-ion intercalation into microcrystalline graphite. *Faraday Discuss.* **172**, 223–237 (2014).

29. Zhao, S. Y. F. et al. Controlled electrochemical intercalation of graphene/h-BN van der Waals heterostructures. *Nano Lett.* **18**, 460–466 (2018).

30. Echeverry, J. P., Chulkov, E. V., Echenique, P. M. & Silkin, V. M. Low-energy collective electronic excitations in LiC_6, SrC_6 and BaC_6. *Phys. Rev. B* **100**, 115137 (2019).

31. Osiander, R., Firebaugh, S. L., Champion, J. L., Farrar, D. & Darrin, M. A. G. Microelectromechanical devices for satellite thermal control. *IEEE Sens. J.* **4**, 525–531 (2004).

32. Jansen, A. N., Amine, K. & Henriksen, G. L. *Low-cost Flexible Packaging for High-power Li-Ion HEV Batteries* Anl-04/09 (Argonne National Laboratory, 2004); https://doi.org/10.2172/828774

Methods

MLG synthesis. MLG was synthesized by chemical vapour deposition (CVD; planarTECH CVD) on 25-μm-thick Ni foils (Alfa Aesar, 12722). First, the Ni foil substrate was heated to a growth temperature of 1,050 °C under 100 s.c.c.m. H_2 and 100 s.c.c.m. Ar flow and annealed at 1,050 °C for 20 min. Then, 35 s.c.c.m. CH_4 flow was used as carbon precursor for 15 min at atmospheric pressure, with addition to 100 s.c.c.m. H_2 and 100 s.c.c.m. Ar flow at 1,050 °C. Finally, the sample was quickly cooled to room temperature under 100 s.c.c.m. H_2 and 100 s.c.c.m. Ar flow. The thickness of the MLG was ~150 layers.

MLG transfer. Polyethylene (20-μm-thick) was laminated on MLG on Ni foil at 160 °C. The Ni was etched in 1 M $FeCl_3$ solution for ~8 h and rinsed with deionized water.

Device fabrication. Aluminium foil coated with Li-NMC ($LiNiMnCoO_2$, 5:3:2) was used as the cathode. Polyethylene (25-μm-thick) porous membrane was placed on top of the NMC layer as a separator. A frame of Cu foil was placed on the porous PE to function as an electrode for the MLG. The MLG transferred on PE was placed on top of the separator with the MLG facing down and in contact with the Cu frame. Battery-grade $LiPF_6$ in ethylene carbonate (EC)/diethyl carbonate (DEC) 1:1 (lithium hexafluorophosphate in EC and DEC from Gelon Energy Co.) was applied to the separator (~250 μl for an area of 3×3 cm²). The device was placed in a PE pouch and vacuum-sealed. For the multispectral display device, Li-NMC-coated Al foil was patterned with a plotter to electrically isolate the pieces from each other. For the sheet resistance measurements, in addition to the above procedure, we placed four additional copper contacts on the corners of the MLG to enable the van der Pauw technique to be carried out.

Spectroscopic characterization. Visible and NIR reflection measurements were performed with a Cary 5000 UV-vis-NIR spectrometer equipped with an integrating sphere. Infrared images and videos were recorded with a FLIR T660 thermal camera. Infrared reflection measurements were carried out using a Perkin Elmer Spectrum 100 FTIR spectrometer equipped with a mid-infrared integrating sphere (PIKE Mid-IR IntegratIR) and a wide-band liquid-nitrogen-cooled mercury-cadmium-telluride detector at a spectral resolution of 4 cm⁻¹. The emissivity values were calculated from the measured reflection spectra: $\varepsilon = 1 - R$. Terahertz reflection measurements were performed using a time-domain terahertz spectrometer (Toptica Teraflash), which uses two InGaAs photoconductive antennas as terahertz transmitter and receiver. The terahertz pulse was guided using a reflection head, which contains four parabolic mirrors to focus the terahertz pulse onto a sample and focus the reflected terahertz pulse back to the receiver antenna. Raman measurements were performed using a Renishaw inVia Raman spectrometer equipped with 457, 488, 514 and 633 nm lasers and ×50 objective. For the sheet resistance measurements, two Keithley 2400 source meters were used: one for charging the device and the other for the four-point resistance measurement. Before charging the device, its sheet resistance was measured following the standard van der Pauw method. The four-point resistance of the device was measured at 5-s intervals for the charging cycle. Charging was interrupted while measuring the device resistance to avoid measurements being affected by the source meter charging the device. Changes in the four-point device resistance and the initial sheet resistance were used to evaluate the curve in Fig. 2d.

Data availability
Data are available from the authors upon request.

Code availability
The custom code used for fitting of the optical reflectivity is available from the authors upon request.

Author contributions
C.K. conceived the idea. M.S.E. synthesized the graphene samples and fabricated the devices. M.S.E., G.B., E.K., O.S., S.B. and C.K. performed the experiments. L.W.L.F., R.P.F., P.S. and X.Y. helped with the fabrication of the devices. V.I.F., K.N. and R.A.W.D. assisted with data analysis and manuscript preparation. G.B., M.S.E. and C.K. analysed the data and wrote the manuscript with input from all the authors. All authors discussed the results and contributed to the scientific interpretation as well as to the writing of the manuscript. VIF and KSN acknowledge support from EU Flagship Programs (Graphene CNECTICT-604391 and 2D-SIPC Quantum Technology), European Research Council Synergy Grant Hetero2D, the Royal Society, EPSRC grants EP/N010345/1, EP/P026850/1, EP/S030719/1.

Competing interests
C.K. is involved in activities towards the commercialization of graphene-based optical surfaces by SmartIR Ltd. The work is subject to a patent application by C.K., M.S.E. and G.B. The remaining authors declare no competing interests.

Additional information
Supplementary information The online version contains supplementary material available at https://doi.org/10.1038/s41566-021-00791-1.

Correspondence and requests for materials should be addressed to C.K.

Peer review information *Nature Photonics* thanks the anonymous reviewers for their contribution to the peer review of this work.

Reprints and permissions information is available at www.nature.com/reprints.